Mechanisms of low-frequency oxygen variability in the North Pacific

Takamitsu Ito [1], Matthew C. Long [2], Curtis Deutsch [3], Shoshiro Minobe [4,5] and Daoxun Sun [1]

[1]Georgia Institute of Technology, Atlanta, Georgia, USA.
[2]Climate and Global Dynamics Laboratory, National Center for Atmospheric Research, Boulder, Colorado, USA.
[3]School of Oceanography, University of Washington, Seattle, Washington, USA.
[4]Department of Natural History Sciences, Graduate School of Science, Hokkaido University, Sapporo, Japan.
[5]Department of Earth and Planetary Sciences, Faculty of Science, Hokkaido University, Sapporo, Japan.

Key Points:

- Two hypotheses are proposed for upper ocean oxygen variability that is synchronized with the Pacific Decadal Oscillation.
- Tropical variability is primarily controlled by the heave of isopycnal surfaces, while the subtropics are controlled by the ventilation.
- Historic observations and a numerical model suggest additional, amplifying mechanisms that enhance tropical oxygen variability.

Corresponding author: Takamitsu Ito, taka.ito@eas.gatech.edu

Abstract

This study investigates the mechanisms of interannual and decadal variability of dissolved oxygen (O_2) in the North Pacific using historical observations and a hindcast simulation using the Community Earth System Model (CESM). The simulated variability of upper ocean (200 m) O_2 is moderately correlated with observations where sampling density is relatively high. The dominant mode of O_2 variability explains 24.8% of the variance and is significantly correlated with the Pacific Decadal Oscillation (PDO) index (r = 0.68). Two primary mechanisms are hypothesized by which the PDO controls upper-ocean O_2 variability. Vertical movement of isopycnals ("heave") drives O_2 variations in the deep tropics; isopycnal surfaces are depressed in the eastern tropics under the positive (El Niño-like) phase of PDO, leading to O_2 increases in the upper water column. In contrast to the tropics, changes in subduction are the primary control on extra-tropical O_2 variability. These hypotheses are tested by contrasting O_2 anomalies with the heave-induced component of variability calculated from potential density anomalies. Isopycnal heave is the leading control on O_2 variability in the tropics, but heave alone cannot fully explain the amplitude of tropical O_2 variability, likely indicating reinforcing changes from the biological O_2 consumption. Mid-latitude O_2 variability indeed reflects ocean ventilation downstream of the subduction region where O_2 anomalies are correlated with the depth of winter mixed layer. These mechanisms, synchronized with the PDO, yield a basin-scale pattern of O_2 variability that are comparable in magnitude to the projected rates of ocean deoxygenation in this century under "unchecked" emission scenario.

1 Introduction

Ocean deoxygenation is generally considered as a direct consequence of ocean heat uptake; as ocean waters warm, dissolved oxygen (O_2) concentrations decline, with profound impacts on marine ecosystems and redox-sensitive biogeochemical cycling [*Breitburg et al.*, 2018]. Surface waters are O_2-rich as concentrations are set to near saturation via air-sea gas exchange; oxygen in the ocean interior is reduced, however, as it is consumed by respiration. The solubility of oxygen in seawater ($O_{2,sat}$) is a function of both temperature and salinity, though it is most sensitive to temperature [*Garcia and Gordon*, 1992]. Oxygen saturation declines by approximately 7 μM with every 1°C increase in temperature; thus, ocean warming drives oxygen loss directly through reduced solubility. Under an increasing greenhouse forcing, however, warming likely progresses from the surface to depth, thereby potentially increasing density stratification in some parts of the upper ocean. Increased stratification weakens vertical mixing of waters, and physical O_2 supply from the surface to interior ocean is predicted to decline. The combination of reduced solubility and diminished vertical exchange are driving ocean deoxygenation on the centennial timescale [*Keeling et al.*, 2010]. Existing observations are starting to reveal the magnitude and pattern of the long-term O_2 decline [*Schmidtko et al.*, 2017; *Ito et al.*, 2017]; however, long-term trends are marked by substantial interannual to decadal fluctuations [*Ito and Deutsch*, 2010; *Long et al.*, 2016].

Numerous studies have documented multi-decadal trends of O_2 in the North Pacific based on ocean time series, repeat hydrography, and compilation of historic datasets [e.g., *Andreev and Baturina*, 2006; *Emerson et al.*, 2004; *Helm et al.*, 2011; *Ono et al.*, 2001; *Sasano et al.*, 2015; *Stramma et al.*, 2008; *Whitney et al.*, 2007]. Most of these studies have focused on a particular site or repeat transects; data coverage is limited both in space and time. In some cases, statistically significant multi-decadal trends have been observed, but attribution of the observed trends to particular forcing(s) is challenging, since O_2 fluctuates naturally due to internally-driven, low-frequency climate variability [*Garcia et al.*, 2005; *Long et al.*, 2016; *Ito and Deutsch*, 2010]. Thus, understanding the natural variability of O_2 itself is an important step towards correct interpretation of observed O_2 changes.

On interannual to decadal timescales, variability of subduction rates impact the physical O_2 supply to thermocline waters [*Kwon et al.*, 2016a; *Mecking et al.*, 2008; *Deutsch et al.*, 2006]. Lateral shifts of water mass boundaries can re-distribute O_2 and nutrient fields, for instance near the subtropical-subpolar front in the northwestern Pacific [*Kwon et al.*, 2016b]. Vertical shifts of water masses impact tropical O_2 variability through the alteration of vertical nutrient supply to the euphotic layer and the associated subsurface respiratory O_2 demand [*Eddebbar et al.*, 2017; *Deutsch et al.*, 2011]. In the subtropical gyres, this coupling between nutrient and O_2 cycles can lead to compensation between physical O_2 supply and biological consumption [*Deutsch et al.*, 2006], while in the tropical ocean, these processes are likely to be reinforcing [*Deutsch et al.*, 2011]. Due to the tight link between these mechanisms and the large-scale circulation, there is a potential for O_2 variability to be coherent over large spatial scales.

The relatively long (decadal) memory of thermocline water masses also creates a tendency for O_2 variability to be elevated on the decadal timescales [*Ito and Deutsch*, 2010], making it difficult to discriminate between anthropogenically forced climate signal and natural fluctuations [*Long et al.*, 2016]. Consequently, our understanding of low-frequency O_2 variability mostly derives from numerical models. State-of-the-art Earth system models still struggle to skillfully simulate present-day O_2 distributions [*Cabré et al.*, 2015]. However, these models are useful because they invoke mechanistic representations of key processes. A major challenge is to calibrate the predictions from numerical model using limited observational data.

The objective of this study is two-fold; First, the pattern O_2 variability is examined in historical O_2 observations and a numerical hindcast simulation on interannual to multi-decadal timescales. Specific attention is paid to the O_2 variability associated with the dominant mode of North Pacific climate variability, the Pacific Decadal Oscillation (PDO). Second, through the analysis of observations and the numerical model, we evaluate a number of hypotheses for mechanisms driving O_2 variability.

The structure of this paper is as follows. The section 2 describes the model, experimental design and the observational dataset used in this study. Section 3 describes the modeled and observed pattern of O_2 variability. Section 4 develops the hypotheses, and tests them in the context of the model output and observational data. The section 5 discusses the implications of our results and concludes the paper.

2 Model and observations

A numerical model is used in conjunction with observations in this study; both present unique challenges. Observational analyses are limited by data sparsity; mechanisms driving variability are difficult to determine from limited state information. Model simulations, on the other hand, permit direct evaluation of mechanisms, but suffer from biases and unresolved processes. The two approaches are thus complementary; analysis of observations can determine O_2 variability for data-rich regions, enabling validation of model solutions. Models can then be interrogated to provide in-depth explanations of the mechanisms driving variability, noting that consistency with limited observations does not guarantee universal model skill. The scope of our analysis consists of a focus on interannual to multi-decadal variability from the 1950s to present. A hindcast simulations of the observational period (1950s to present) forced by reconstructed atmospheric conditions is performed. Below we first outline the modeling approaches followed by the description of the observational dataset.

2.1 A hindcast simulation using the CESM-BGC

We analyze a "hindcast" integration conducted with the ocean and sea ice components of the Community Earth System Model (CESM) [*Yeager et al.*, 2018]. The CESM

ocean component, the Parallel Ocean Program, version 2 (POP) [*Danabasoglu et al.*, 2012], was integrated at a nominal horizontal resolution of $1^\circ \times 1^\circ$; biogeochemistry was simulated by the Biogeochemical Elemental Cycle (BEC) model [*Moore et al.*, 2013]. BEC represents multiple nutrient co-limitation (N, P, Si, and Fe) and includes three explicit phytoplankton functional groups (diatoms, diazotrophs, and "small" pico/nano phytoplankton), and one implicit group (calcifiers) [*Moore et al.*, 2004]. The model simulates sinking particulate matter, subject to ballasting by mineral dust, biogenic calcite and Si following *Armstrong et al.* [2002]. Iron inputs include atmospheric deposition and sedimentary iron, which is applied using subgrid-scale bathymetry as described by *Moore and Braucher* [2008].

The simulation used here is the forced ocean-sea-ice experiment described in *Yeager et al.* [2018]; it was forced under the Coordinated Ocean-Ice Reference Experiment (CORE) protocols, using inter-annually varying forcing (IAF) deriving from reanalysis and satellite products [*Griffies et al.*, 2009; *Large and Yeager*, 2009]. The CORE forcing was modified in order to correct a spurious trend in tropical Pacific winds evident in the NCEP reanalysis [*Kalnay et al.*, 1996] upon which CORE is based: the winds between 30°S–30°N were replaced with those from the 20th century reanalysis [*Compo et al.*, 2011] (1948–2010) or a modified version of the Japanese 55-year Reanalysis (JRA55) [*Onogi et al.*, 2007] (to extend the simulation to 2015). Further details are provided in *Yeager et al.* [2018].

Figure 1 compares simulated O_2 distributions with the climatological observation based on the World Ocean Atlas 2013 [*Garcia et al.*, 2014]. The modeled O_2 climatology is based on the simulation period of 1948–2015. While the model captures the general pattern of dissolved O_2 distribution reasonably well, it simulates oxygen minimum zones (OMZs) that are too extensive as with most coarse resolution ocean general circulation models. A widespread negative bias of O_2 exists in the thermocline, and its amplitude generally increases with depth. While this is not desirable, it does not preclude using CESM as a research tool, especially at the shallower depths of 100 to 200 m where the model bias is relatively small. Indeed, while O_2 tends to be biased low in the model, the large-scale spatial distribution is well simulated [*Long et al.*, 2016]. The OMZ biases are partially attributable to sluggish circulation yielding weak ventilation [*Brandt et al.*, 2008, 2012; *Dietze and Loeptien*, 2013; *Getzlaff and Dietze*, 2013; *Duteil et al.*, 2014]. The extent of OMZs is also sensitive to the prescribed remineralization profile for sinking organic matter, as well as the stoichiometric ratios used for growth and remineralization of organic matter [*Devries and Deutsch*, 2014]. An additional factor in these biases may be a poor representation of diapycnal mixing over rough topography, particularly in the North Pacific, for instance [*Nakamura et al.*, 2006], which can modulate high latitude O_2 supply.

2.2 Observational analysis based on the World Ocean Database 2013

Beyond the climatological mean distribution of O_2, the temporal evolution of O_2 can be examined using the historic datasets. The World Ocean Database 2013 version 2 [WOD13; *Boyer et al.*, 2013] is a compilation of historic oceanographic measurements submitted by scientists and data managers from the international oceanographic community. Bottle O_2 samples are sparse and irregular, so available samples are binned into a global $5^\circ \times 5^\circ$ longitude-latitude grid cells at monthly intervals. Because of the coarse resolution, data gaps between grid cells are not filled by interpolation. A monthly climatology is constructed for the relatively data-dense period of 1954–2010, and anomalies from the monthly climatology are also computed at monthly intervals. Figure 2A visualizes the yearly sample count for each bin at 200 m averaged over the 57-year period. The data coverage is sparse and uneven, and the sampling density is particularly low in remote regions such as the central subtropical gyres. The sampling density is relatively higher in the western and eastern Pacific.

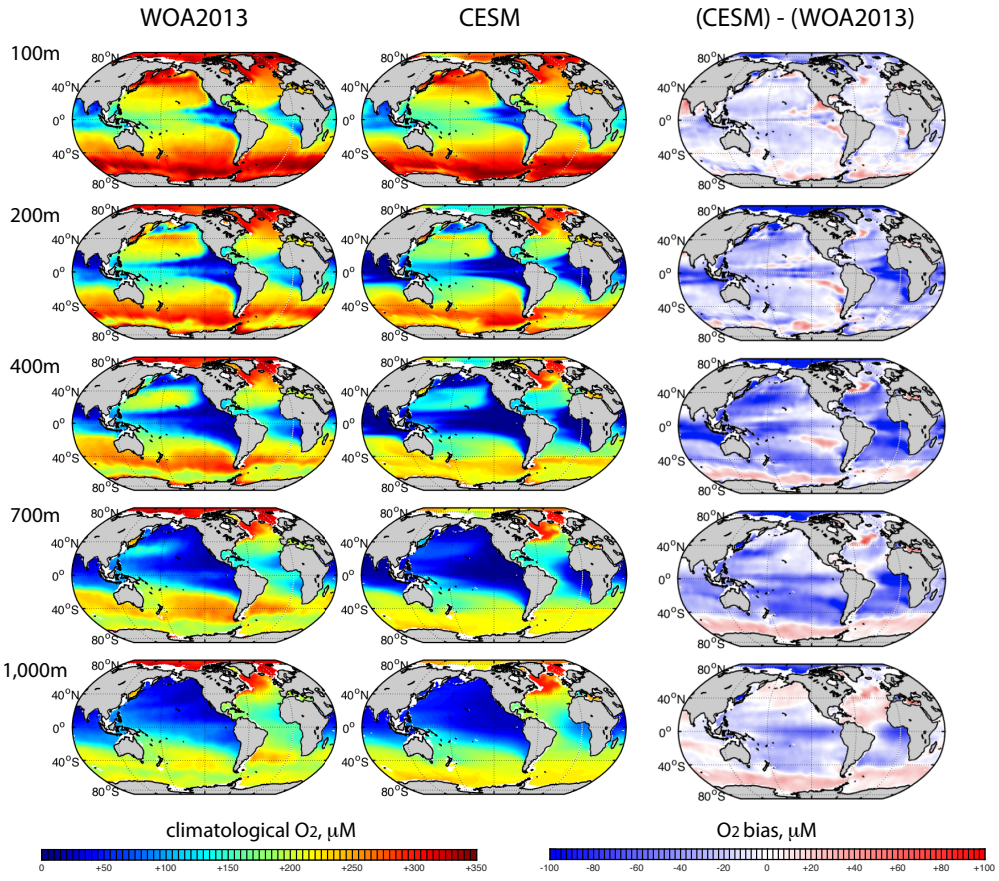

Figure 1. Global O_2 climatology at the depth of 100, 200, 400, 700, and 1,000m based on (left) the World Ocean Atlas 2013 [*Garcia et al.*, 2014] and (center) simulated by the CESM. The right column shows the difference; (observation) - (model).

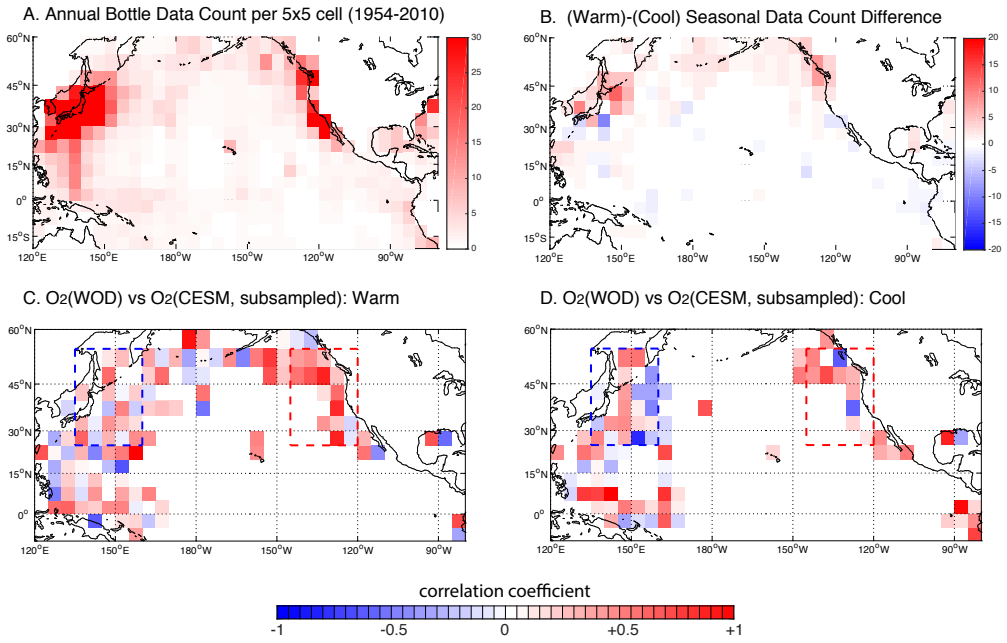

Figure 2. (A) Yearly sample count for each bin at 200 m averaged over the 57-year period from 1954 to 2010. (B) The difference in seasonal sample count at 200 m between warm (April to September) and cool seasons (October to March). (C) Correlation coefficient between observed and simulated O_2 at 200 m in the warm seasons (April-September). The simulated O_2 are subsampled according to the seasonal data count for each bin. Bins with less than 15 years of data coverage are not plotted. In the western Pacific box (blue dash), median correlation is 0.15. In the eastern Pacific box (red dash) the median correlation is 0.30. (D) Correlation coefficient between observed and simulated O_2 at 200 m in the cool seasons (October-March). In the western Pacific box (blue dash), median correlation is 0.06. In the eastern Pacific box (red dash) the median correlation is 0.03.

The data is also uneven temporally. Monthly O_2 anomalies are seasonally or annually averaged because there are too many temporal data gaps at monthly timescale. Figure 2B shows the difference in seasonal sample count at 200 m between warm (April to September) and cool seasons (October to March). It reveals the seasonal bias towards warm seasons in the Subpolar North Pacific poleward of 40°N. On the decadal timescale, O_2 is more frequently sampled between 1960s and 1980s relative to other periods ranging from 2,000 to 3,500 sample count for the equatorial and North Pacific region (120°E–70°W, 20°S–60°N, supplementary Figure 1). Regional sample count decreases to approximately 1,500 samples per year after 1990s. For the most recent periods, not all samples are reported yet, which explains relatively low data count.

Figure 2CD visualizes the local correlation between the modeled and observed O_2 anomalies. The model output is first monthly averaged and interpolated to 200 m on a $5° \times 5°$ longitude-latitude grid commensurate with the observations. Then monthly O_2 anomalies are subsampled according to the monthly sample count of the O_2 observations. In the relatively data-rich regions of the western and eastern Pacific, there is a moderately positive correlation between the modeled and observed O_2 anomalies in the warm seasons (0.15 in the western Pacific, 0.30 in the eastern Pacific) but the correlation diminishes in the cool seasons, likely reflecting seasonal sampling bias. Annual O_2 anomalies show similar correlation pattern to the warm season with a slightly weaker correlation of 0.13 in

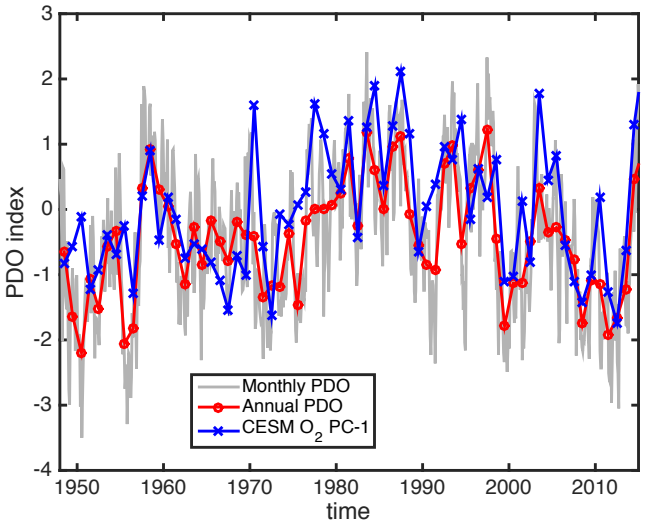

Figure 3. Time series of the first principal component of North Pacific O_2 at the depth of 200 m (blue) is overlaid with the monthly (grey) and annual (red) indices of the Pacific Decadal Oscillation.

the western box and 0.26 in the eastern box. Because the results from the warm season and annual O_2 anomalies are generally similar, our analysis is hereafter focused on annual O_2 anomalies.

3 Simulated and observed O_2 variability

The atmospheric forcing used in the CESM hindcast enables the simulation of the characteristic SST variability associated with the PDO [*Minobe*, 1997; *Mantua et al.*, 1997]. In order to extract dominant modes of the simulated O_2 variability, an empirical orthogonal function (EOF) analysis is performed on the modeled O_2 anomalies at 200 m depth. The North Pacific domain bounded by the 20°N line and the Bering Strait is used for the EOF analysis. Linear trends are removed from each grid cell, and the anomaly values are weighted by the square root of the cosine of latitude to account for the meridional variation in the cell area.

Figure 3 shows the first principal component (PC1) time series of the upper ocean O_2 (at 200 m) overlaid with the indices of PDO with zero lag (red). The PC1 of North Pacific O_2 explains 24.8% of the total variance in this field, and is significantly correlated with the PDO index (r = 0.68, significant at 95% confidence level). The PDO is defined as the leading principle component of monthly sea surface temperature (SST) in the North Pacific, poleward of 20°N [*Mantua et al.*, 1997]. The PDO index is based on the Extended Reconstructed Sea Surface Temperature (ERSST) version 4 [*Huang et al.*, 2015].

The model suggests that there is a coherent, basin-scale pattern in O_2 variability associated with the PDO; the structure of this pattern is consistent with the compilation of WOD13 observations (section 2.2), though significant data gaps at subtropical and tropical latitudes are evident (Figure 4). Figure 4 shows annual O_2 anomalies regressed onto the PDO index based on the observed O_2 anomalies (Figure 4A), full model output (Figure 4B) and subsampled model output (Figure 4C). The plotted values are the regression coefficients, measuring the rate of change of the dissolved oxygen concentration per one standard deviation increase in the PDO index. Similar to Figure 2, the model output is re-

gridded to the same resolution ($5^\circ \times 5^\circ$) as binned observations at seasonal and annual timescale. For Figure 4C, the model output is then subsampled at monthly intervals according to the existence of bottle O_2 samples in WOD13. Note that Figure 4 only shows the annual anomalies because the basic structure remains consistent with the seasonal analysis (shown in supplementary Figure 2).

The pattern correlation between the panel A and C of Figure 4 is only moderate, $r = 0.25$, but the model reproduces several large scale features. In the positive phase of PDO, O_2 tends to be elevated in the eastern tropics, central/western subtropics, and eastern boundary current region. Conversely, the O_2 tends to be lower in the western tropics and western subpolar region under the positive PDO. Both full and subsampled model output show the elevated O_2 under the positive PDO in the eastern tropics, central/western subtropics and the eastern boundary upwelling region, similar to the observation. It also reproduces the lower O_2 in the off-equatorial western tropics under the positive PDO. The strip of positive relationship is well captured in the eastern boundary region along the west coast of North America. The model shows negative relationship in the western subpolar region and in the Bering Sea, consistent with the observations. There is also a region of negative correlation between the central subtropics and the eastern boundary region. Subsampling makes the pattern more noisy but the basic patterns are robust. Overall the model correctly captures the broad structure of the relationships between the PDO and O_2 while it appears to slightly underestimate its amplitude. In the next section, the possible mechanisms controlling the O_2 variability are discussed in the context of this model hindcast simulation.

4 Hypotheses: Isopycnal Heave and Subduction

Figure 5 illustrates two basic hypotheses driving the O_2 variability. The first hypothesis is that O_2 variability in the low latitude thermocline is driven primarily by the adiabatic vertical displacement of isopycnals, termed "heave." At low latitudes, the water column is strongly stratified with warm, O_2-rich waters overlying cold, O_2-poor waters at depth. As the water masses age in the subsurface, O_2 is depleted due to the cumulative effect of respiration, which can be estimated with Apparent Oxygen Utilization (*AOU*).

$$AOU = O_{2,sat}(S,T) - O_2 \tag{1}$$

Even though the O_2 solubility is lower in the warmer surface waters, it contains more O_2 because of small *AOU* relative to the old deep waters. Isopycnal displacements translate this background gradient into the anomalies observed at a constant depth, such that (in most cases) downward motions yield elevated O_2 and upward motions reduced O_2. In the positive (El-Niño like) phase of PDO, the zonal tilt of the equatorial thermocline is weakened, leading to a downward shift of isopycnals and an O_2 increase in the eastern equatorial Pacific. An upward shift of isopycnal surfaces in the western equatorial Pacific leads to an decrease in O_2 there. This mechanism is consistent with the tropical zonal dipole equatorward of 15°N as shown in Figure 4.

At mid and high latitudes, subsurface O_2 is enriched in the vicinity of water mass formation as the downward movement of water supplies O_2 to the ocean interior. The second hypothesis is that the dominant mechanism for mid/high-latitude O_2 variability is variation in subduction, which is the transfer of mixed layer waters into the thermocline as illustrated in Figure 5B. At mid/high latitudes, the climatological vertical gradients of density and oxygen are relatively weak; oxygen is brought into the thermocline by the subduction of cold, O_2-rich waters during deep winter mixing. The strength of subduction can be modulated by climate variability, such as the strength of winter-time cooling and anomalies in circulation. A stronger cooling and deeper winter-time mixing can increase the supply of O_2 to the thermocline. In contrast, a warmer and shallower mixed layer can weaken the O_2 supply. These hypotheses will be tested in the context of the observation and the model output.

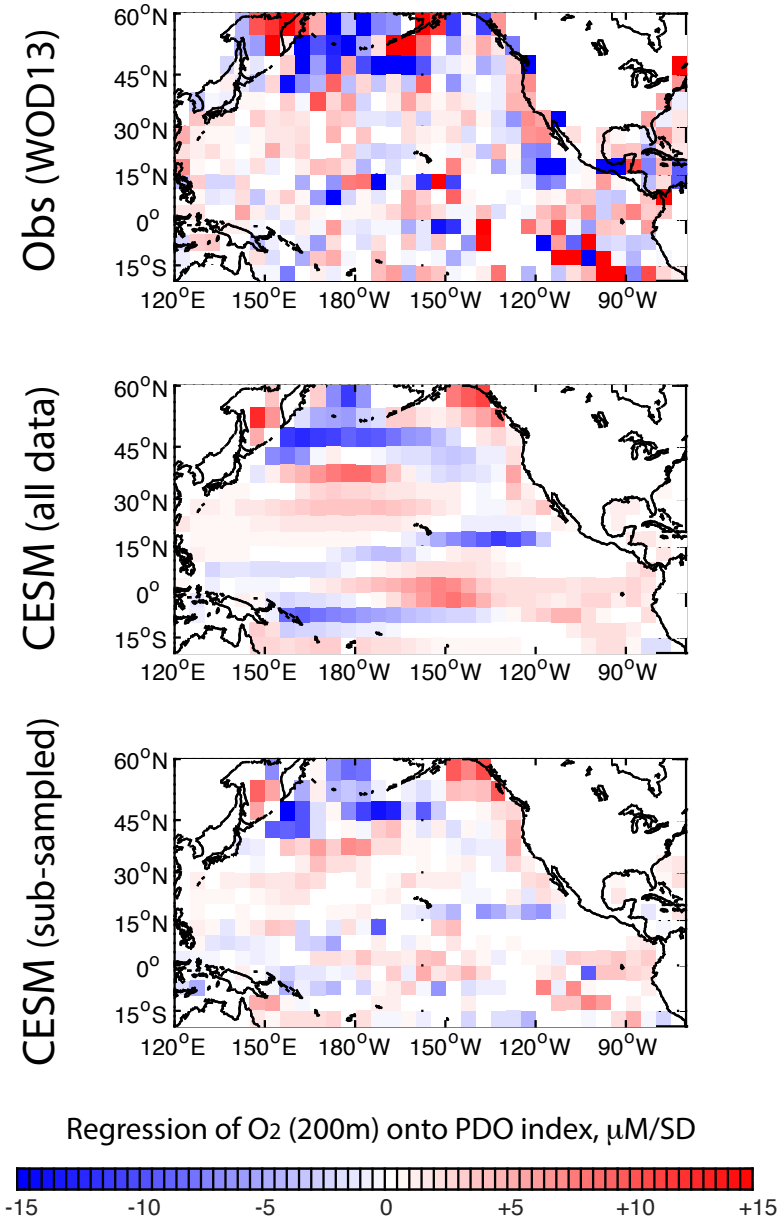

Figure 4. (A) The observed pattern of O_2 at 200 m depth associated with the PDO calculated as a regression coefficient in the units of μM per one standard deviation of the PDO index (μMSD^{-1}). The plotted values are the regression coefficients, measuring the rate of change of the dissolved oxygen concentration per one standard deviation increase in the PDO index. (B) Same as (A) but for the full model output. (C) Same as (A) but for the subsampled model output. Pattern correlation between panel (A) and (C) is 0.25.

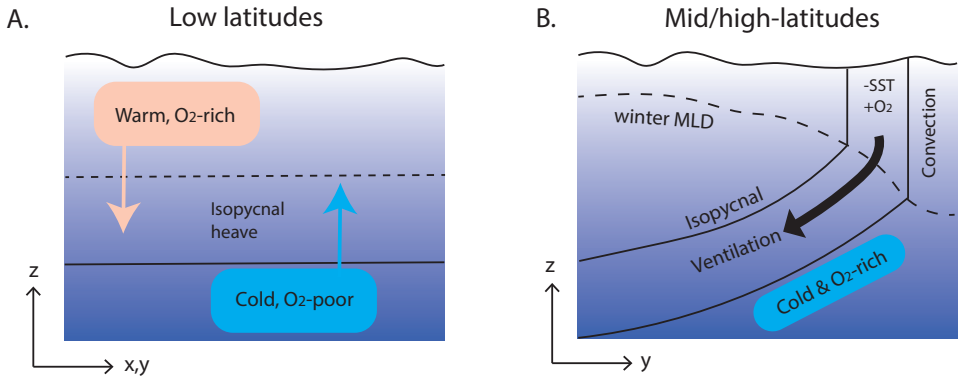

Figure 5. Schematic illustration of our hypotheses. (A) At low latitude, interannual variability of O_2 is influenced by isopycnal heave, leading to a positive correlation between O_2 and heat content. (B) At mid/high-latitudes, O_2 content increases due to physical O_2 supply from winter-time convection and subduction, yielding a negative correlation between O_2 and heat. Atmospheric teleconnections and thermocline adjustments may link these changes across large distances.

4.1 Upper ocean physical properties and the PDO

We use the model output to examine the hypothesized mechanisms behind the O_2 variability. Physical circulation changes associated with the PDO is first calculated and displayed in Figure 6 including the anomalies of (A) winter-time mixed layer depth, (B) winter-time zonal wind stress, (C) meridional overturning circulation of the Indo-Pacific basin and (D) vertical displacement of isopycnals at 200 m depth. All anomalies are calculated relative to the monthly climatology and are averaged for January-Februrary-March for the winter-time quantities and for all months otherwise.

Figure 6A shows a widespread deepening of the winter mixed layer under the positive phase of PDO in the western/central subtropical Pacific from 150°E to 150°W and 30°N to 45°N. This is consistent with the stronger westerly wind as shown in Figure 6B, which drives stronger heat loss and deeper convective mixing during cold seasons. The relationship between variation in subduction rates and the PDO is established in an eddy-resolving model of the North Pacific [*Qu and Chen*, 2009], where the deepening of the winter MLD is closely linked to the atmospheric forcing of air-sea heat flux and the surface wind speed. Figure 6B also shows a moderate weakening of trade winds over the western/central equatorial Pacific, which appears as a westerly anomaly. The response of the meridional overturning circulation (MOC) in the Indo-Pacific basin is calculated as the difference between the global and the Atlantic MOC (Figure 6C), highlighting the weakened tropical upwelling under the positive phase of PDO.

In the El-Niño like, positive phase of PDO, the thermocline deepens in the eastern equatorial Pacific and it shoals in the western tropical Pacific (Figure 6D). The vertical displacement of isopycnals are calculated based on the potential density anomalies according to the following formula at 200 m depth,

$$z' = -\left(\frac{\partial \overline{\rho_\theta}}{\partial z}\right)^{-1} \rho'_\theta \tag{2}$$

where a positive (negative) z' indicates a shoaling (deepening) of isopycnal with a positive (negative) potential density anomaly. Overlines indicate climatological annual means, and primed quantifies are the anomalies from the mean climatology.

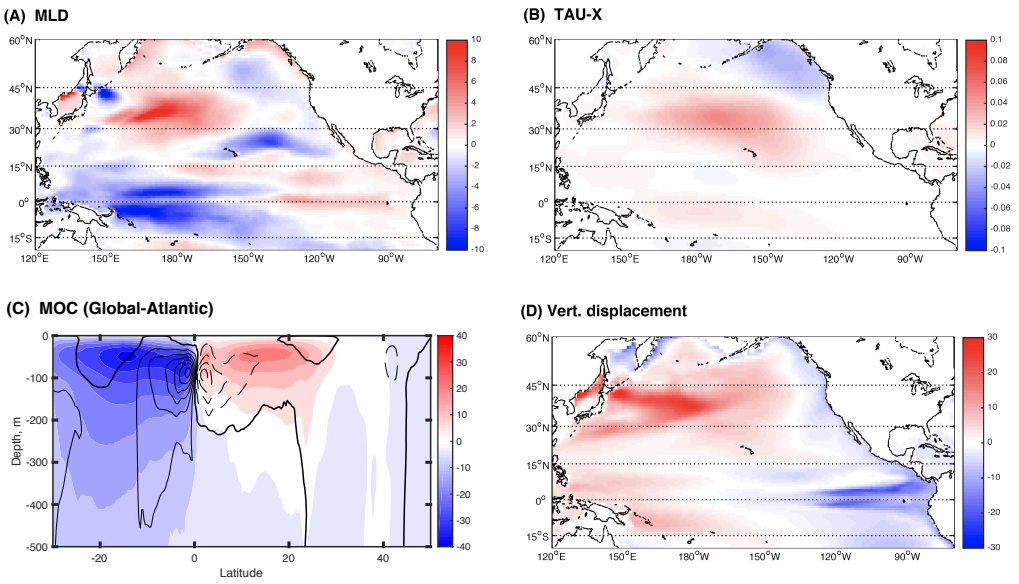

Figure 6. Simulated physical properties regressed onto the PDO index. (A) regression coefficient for the winter-time mixed layer depth in units of m SD^{-1} where the regression coefficient is scaled per one standard deviation (SD) of the PDO index. The plotted regression coefficients measure the rate of change of the winter-time mixed layer depth per one standard deviation increase in the PDO index. The winter season average is defined as the averages of January, Februrary and March. (B) same as (A) but for the winter-time zonal wind stress in units of Pa SD^{-1}. (C) same as (A) but for the Indo-Pacific MOC. Color shading is the climatological MOC. Black solid lines indicate positive regression coefficients of Indo-Pacific MOC in units of Sv SD^{-1} whose contour interval is set to 0.5 Sv SD^{-1}. Black dash contour indicate negative regression coefficients with the same interval. (D) same as (A) but for the vertical displacement of isopycnal layers at 200 m depth in units of m SD^{-1}. Vertical displacement is positive upward; a positive (negative) displacement indicates deepening (shoaling).

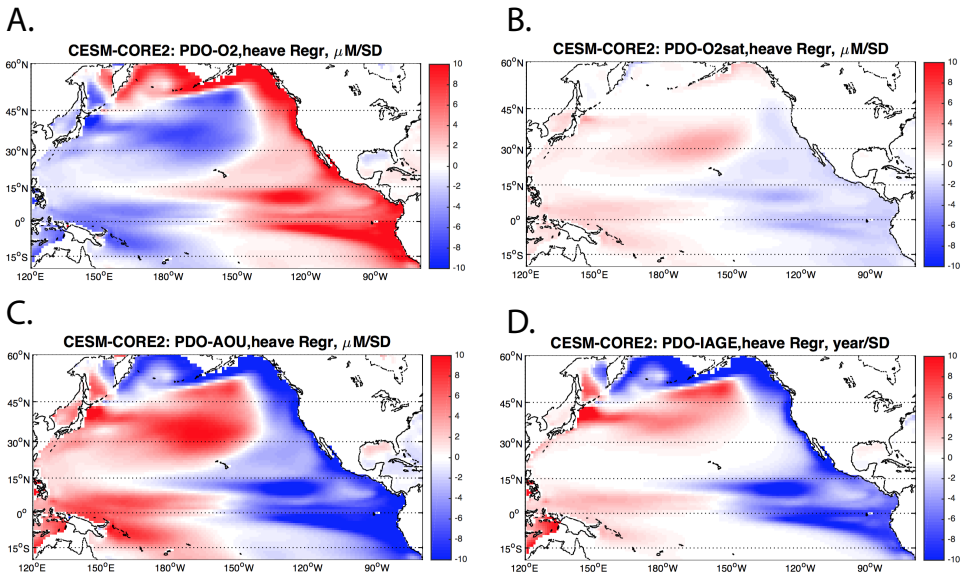

Figure 7. Heave-induced O_2 - PDO relationship. (A) Heave-induced O_2 anomalies regressed onto the PDO index in the units of μM per one standard deviation of the PDO index (SD^{-1}). The plotted regression coefficients measure the rate of change of the heave-induced O_2 anomalies per one standard deviation increase in the PDO index. (B) Same as (A) but for $O_{2,sat}$. (C) Same as (A) but for *AOU*. O_2 is negatively proportional to *AOU* by definition. (D) Same as (A) but for ideal age tracer in the units of yr SD^{-1}. The anomalies are calculated on the annual timescale, and is regressed onto the annual PDO indices.

In the western/central subtropics, the thermocline shoals (deepens) under the positive (negative) phase of PDO. While Figure 6C shows weakened subtropical overturning cell under the positive phase of PDO, the subtropical thermocline appears to be ventilated stronger due to the stronger westerly wind and deeper winter mixed layer.

4.2 Isopycnal heave and tropical O_2 variability

In order to quantify the effect of isopycnal heave, we calculated the heave-induced O_2 anomalies at each grid point as:

$$O'_{2,heave} = \left(\frac{\partial \overline{O_2}}{\partial z}\right)\left(\frac{\partial \overline{\rho_\theta}}{\partial z}\right)^{-1} \rho'_\theta \tag{3}$$

where ρ_θ is the potential density with respect to the surface pressure. Overlines indicate climatological annual means, and primed quantifies are the anomalies from the mean climatology. Heave-induced anomalies of other relevant tracers ($O_{2,sat}$, *AOU*, ideal age tracer) are also computed for each year.

Figure 7A shows the simulated, heave-induced O_2 anomalies ($O'_{2,heave}$) regressed onto the PDO index. It shares a similar pattern with the vertical displacement (Figure 6D). An increase in $O'_{2,heave}$ occurs under the deepening of isopycnals. Fig 5A, 6D and Figure 7A together suggest that the heave effect can reproduce the correct pattern of O_2 change at low latitudes. For example, the downward shift of isopycnals in the eastern tropical Pacific brings down the relatively high O_2 from above, leading to the positive O_2 anomaly

under the positive phase of PDO. Indeed, the heave-induced O_2 changes (Figure 7A) can quantitatively reproduce the O_2 change (Figure 4D) equatorward of 15°N. However, similar comparison in the subtropics suggests that heave-induced O_2 is not a good indicator of the net O_2 change there. Heave-induced O_2 anomalies do not explain the positive relationship between O_2 and PDO in the central/western subtropics and most of the O_2 anomalies north of 15°N.

Figure 7BCD further illustrates the mechanism behind the heave-induced O_2 changes. The heave-induced $O_{2,sat}$ and AOU oppose one another but the magnitude of AOU dominates the net O_2 change. Changes in AOU closely follows the changes of ideal age tracer (Figure 7D), suggesting the important role of water masses with different water ages in controlling the AOU variability.

4.3 Subduction and subtropical O_2 variability

In the central/western subtropics, both the observation and the model show that O_2 is positively correlated with the PDO index (Figure 4). However, the heave-induced O_2 is negatively related to the PDO index in this region (Figure 7A). This implies that the non-heave component of O_2 anomalies associated with the PDO must be strongly positive in order to overcome the heave-induced negative O_2 anomalies. The non-heave component of O_2 variability can be calculated as the residual O_2 anomaly ($O'_{2,residual}$ = O'_2 - $O'_{2,heave}$) using both observations and model output. To calculate $O'_{2,residual}$ using WOD13, potential density of each bottle sample is first calculated and is averaged within the 5° × 5° longitude-latitude bins. Observed $O'_{2,heave}$ is calculated applying the Eq 3 to the observed potential density anomalies and climatological vertical gradients. To examine the effect of sparse sampling, the model output is also binned and subsampled at the same resolution.

Figure 8A-C shows the $O'_{2,residual}$ regressed onto the PDO index using observations, full model output, and subsampled model output at annual interval. Same analyses are repeated using seasonal data (supplementary Figure S3), and the results are essentially the same as the annual product. The pattern correlation between the panel A and C of Figure 8 is only moderate, $r = 0.14$, but there is a common response in the subtropics. It shows a strong positive response to the PDO in the western/central subtropical Pacific with the amplitude of ~15μM per SD. This pattern is consistent with the anomalously deep winter mixed layer shown in Figure 6A and its influence on the increased ventilation. Stronger ventilation associated with the PDO drives increased O'_2 in the subtropics, but other processes merit consideration; in particular, SST variability will impact O_2 solubility and shifts in export production might alter biological O_2 utilization. In the central/western subtropics, SST is cooler by ~-0.4°C per SD of the PDO leading to a solubility increase of ~3μM per SD, much smaller than the amplitude of $O'_{2,residual}$ associated with the PDO in Figure 8. Taken together this result is supportive of the mid-latitude hypothesis (Figure 5B) for the positive relationship between the subtropical O_2 and PDO.

Regression of $O'_{2,residual}$ (Figure 8A) is quite noisy in the central and eastern equatorial Pacific, and it is difficult to draw a definitive conclusion there. In the western equatorial Pacific, simulated $O'_{2,residual}$ is positively correlated with the PDO. These regions of the deep tropics are not close to the region of subduction, thus it is likely that shift in biological O_2 utilization may provide alternate explanation for these anomalies. The positive correlation indicate weakened biological O_2 consumption that leaves behind higher level of O_2.

To further examine the cause of tropical $O'_{2,residual}$ pattern, the rates of biological O_2 utilization (Oxygen Utilization Rate, OUR) are diagnosed in the model at 200 m (Figure 9) and regressed onto the PDO index. The regression coefficient shows that the biological O_2 consumption weakens in the tropics and strengthens in the subtropics. There is a zonally elongated region with negative regression coefficients from approximately 150°E to 150°W and 5°S to 5°N spanning much of the central and western equatorial Pacific.

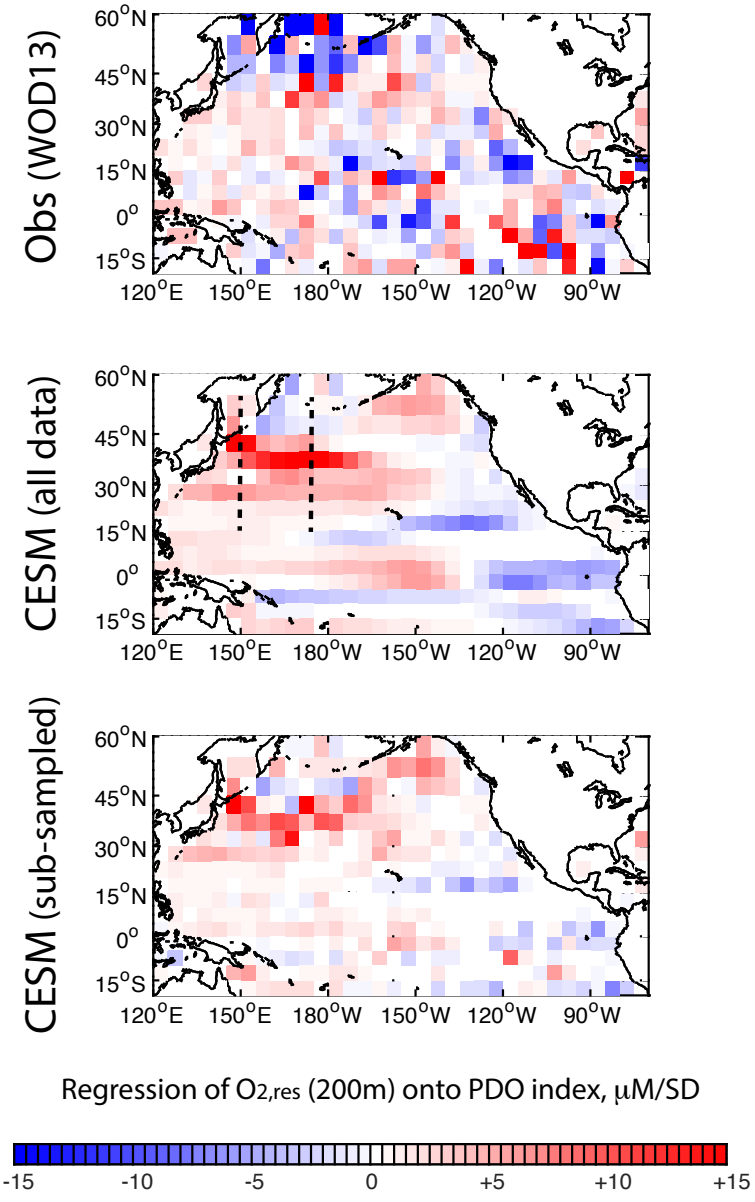

Figure 8. Residual O_2 - PDO relationship as calculated by the regression coeffcient between the $O'_{2,residual}$ and the PDO indices in the units of μMSD^{-1}. The plotted regression coefficients measure the rate of change of the residual O_2 anomalies per one standard deviation increase in the PDO index. Dash lines in panel (B) indicate the location of transect shown in Figure 11. Pattern correlation between panel (A) and (C) is 0.14 for the plotted region.

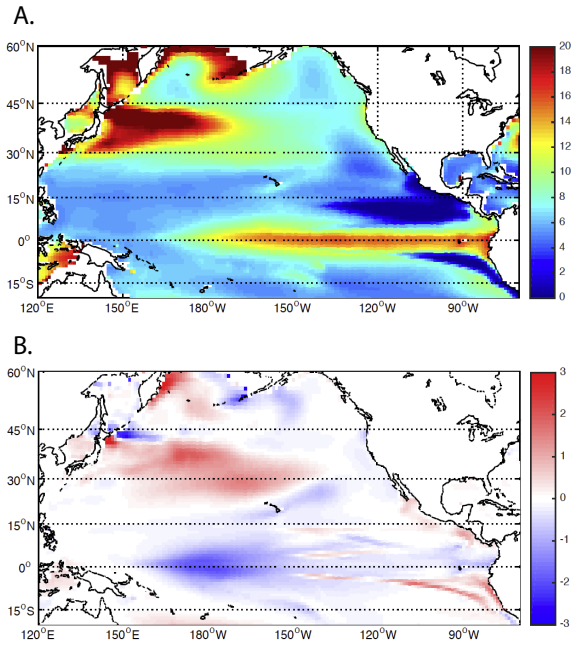

Figure 9. (A) Climatological annual mean OUR at 200 m depth in the units of μM yr^{-1} (B) Regression coefficient of OUR anomalies at 200 m onto the PDO index, μM yr^{-1} SD^{-1}. The plotted regression coefficients measure the rate of change of the OUR anomalies per one standard deviation increase in the PDO index.

This change can explain the positive correlation between $O'_{2,residual}$ and the PDO in the tropics where the increase of O_2 beyond the effects of isopycnal heave may be caused by the weakened biological O_2 consumption [*Palter and Trossman*, 2018]. In contast, there is an increased OUR in the central and western subtropical North Pacific (150°E to 150°W and 25°N to 40°N). This is likely due to the increased entrainment of nutrients due to the deeper winter mixed layer. Increased biological productivity can increase the O_2 consumption and lower the O_2 concentration. However, the pattern of $O'_{2,residual}$ regression on to PDO is broadly positive, indicating that ocean ventilation still dominates the O_2 variability there.

In summary, the two hypotheses, isopycnal heave and ventilation, have distinct regional expressions associated with the PDO. O'_2 generated by isopycnal heave reflects the re-distribution of O_2 within the ocean, and it dominates the low latitude O_2 variability. It is obvious that these hypotheses cannot fully explain the observed and modeled O_2 variability due to the modulation of OUR by the climate variability. In particular, the positive signal in $O'_{2,residual}$ regression is clearly evident in the western tropics. This tropical signal, however, contains a high level of noise on the seasonal timescale (supplementary Figure S3) likely due to the sparse sampling. While $O_{2,heave}$ plays a major role in the tropics, it is not the only mechanism of the O_2 variability there. The effect of ventilation primarily controls the subtropical O_2 variability. In both tropics and subtropics, the changes in $O_{2,sat}$ is relatively weak and the net O_2 changes are primarily driven by the changes in AOU.

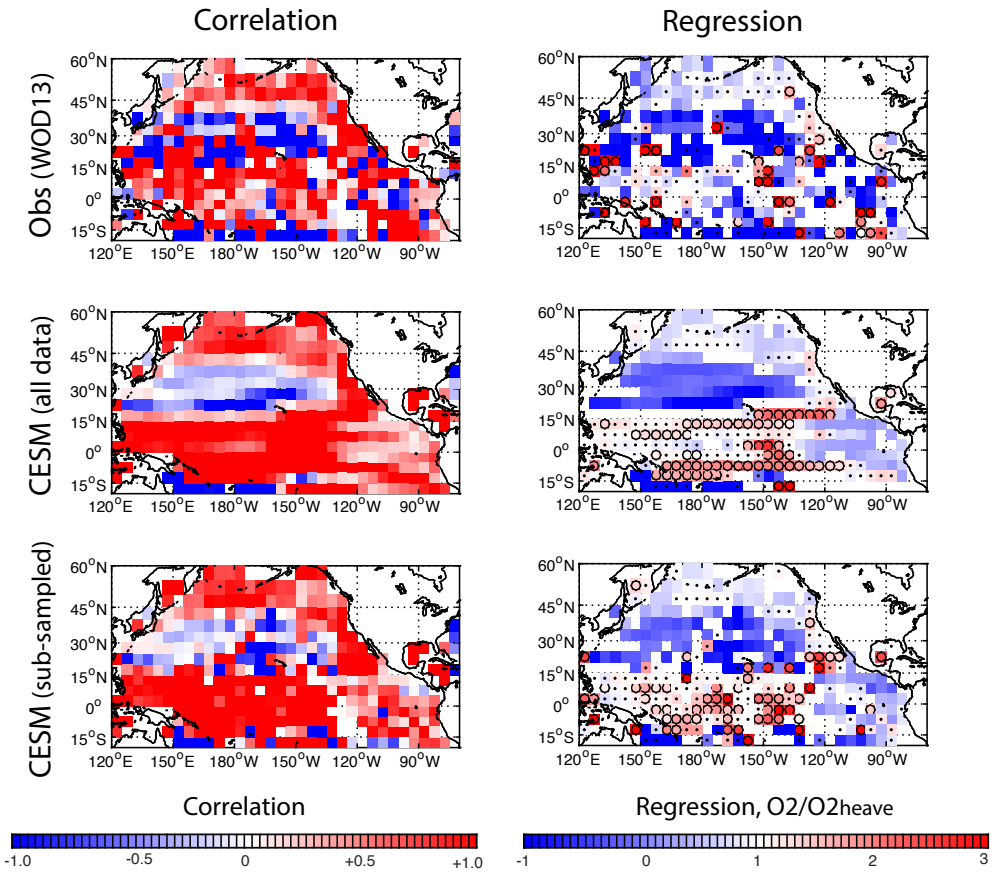

Figure 10. (left column) Local correlation coefficients between O_2 and $O_{2,heave}$ at the depth of 200 m. (right column) Local regression coefficients. O_2 is regressed onto $O_{2,heave}$ and so its regression coefficients are unitless. The plotted regression coefficients measure the rate of change of the O_2 anomalies as a function of changes in the heave-induced O_2 anomalies. (top) Plotted values are from the WOD13 data, (middle) from the full model output, and (bottom) from the subsampled model output. Closed dots indicate that the regression coefficient is not significantly different from 1. Open circles indicate that the regression coefficient is significantly greater than 1. Statistical tests (t-test) are performed at each grid cell using effective degrees of freedom [*Bretherton et al.*, 1999] at the 90% confidence level.

4.4 Testing the hypothesis

So far we have examined the hypotheses in the context of O_2 variability associated with the PDO. Here we perform statistical tests for the general relationship between $O_{2,heave}$ and O_2 anomalies. First, correlation coefficients between O_2 and $O_{2,heave}$ are calculated using modeled and observed data at the depth of 200 m as shown in Figure 10 (left column). Both observations and the model agree that the correlation is predominantly positive except for the central and western subtropical gyre. Subpolar North Pacific poleward of 40°N is also dominated by the positive correlation. The region of negative correlation is consistent with the strong imprint of ventilation associated with the PDO. Here, the relationship between O_2 and $O_{2,heave}$ are including all anomalies but not limited to the perturbations associated with PDO. $O_{2,heave}$ has a positive relationship with temperature where colder, deeper water is relatively depleted in O_2 in the climatological sense.

The negative correlation in the central and western subtropics reflects the inverse relationship betweeen temperature and O_2. Colder and denser surface waters tend to promote the winter-time mixing and ventilation of the thermocline, thus increasing subsurface O_2. The meridional transects of composite O_2 (Figure 11) also show the effect of ventilation. The locations of these two transects are marked as dash lines in Figure 8. Contour lines indicate composite O_2 anomalies associated with the PDO. The composite O_2 anomalies are calculated by taking the difference of O_2 between the positive PDO ($> +1$) and the negative PDO (< -1) states. One standard deviation (SD) is used as the threshold for positive/negative PDO, and they show the strong positive anomaly in the region of subduction and the newly formed mode waters at 35-40°N.

In the regions where O_2 and $O_{2,heave}$ are positively correlated, we can further examine whether the amplitude of O_2 variability is correctly accounted for by $O_{2,heave}$. This can be tested by locally regressing O_2 anomalies onto $O_{2,heave}$, and examine the regression coefficient. The strict application of the hypothesis predicts a regression coefficient of 1. If it is greater than 1, $O_{2,heave}$ cannot fully explain O_2 variability and additional reinforcing mechanisms, such as biological O_2 consumption, are implied. Similarly, if it is smaller than 1, compensating mechanisms, such as ventilation, are implied.

Figure 10 (right column) shows the pattern of regression coefficient at 200 m. The color scale is set to a neutral color at the regression coefficient of 1. Dots are placed for the $5° \times 5°$ bins whose regression coefficients are not different from 1 with the confidence level of 90% with the degree of freedom set to $N - 2$ with N being the effective sample size following *Bretherton et al.* [1999]. A relatively low confidence level of 90% is used to capture signals with limited data. Circles indicate the bins where regression coefficients are significantly greater than 1. No symbols indicate the bins where regression coefficients are significantly less than 1. For these cases the hypothesis is rejected. Generally, tropics are characterized by the regression coefficient of 1 or greater, thus the heave hypothesis cannot fully explain the observed O_2 variability.

In the observations, the areal extent of regions where O_2 and $O_{2,heave}$ are positively correlated cover 6.9×10^7 km^2 (approximately 65% of the total area) in the Pacific basin within 20°S to 60°N. Negative correlations covers 3.8×10^7 km^2, which is approximately 35% of the total area. Regression coefficients are not significantly different from 1 over 62% of the positively correlated area (4.3×10^7 km^2). In some regions, regression coefficients are significantly greater than 1 (15% of the positively correlated area, 1.0×10^7 km^2). While this is a relatively small fraction for the North Pacific, this analysis revealed that the isopycnal heave cannot fully describe the O_2 variability in these regions, primarily focused in the tropics. CESM shows similar patterns in both full and subsampled outputs in Figure 10(middle and bottom row). The model shows strongly positive correlation in the western and central tropical Pacific. Consistent with the observation, a relatively small fraction of the positively correlated regions in the full and subsampled model output exhibits regression coefficients that are significantly greater than 1.

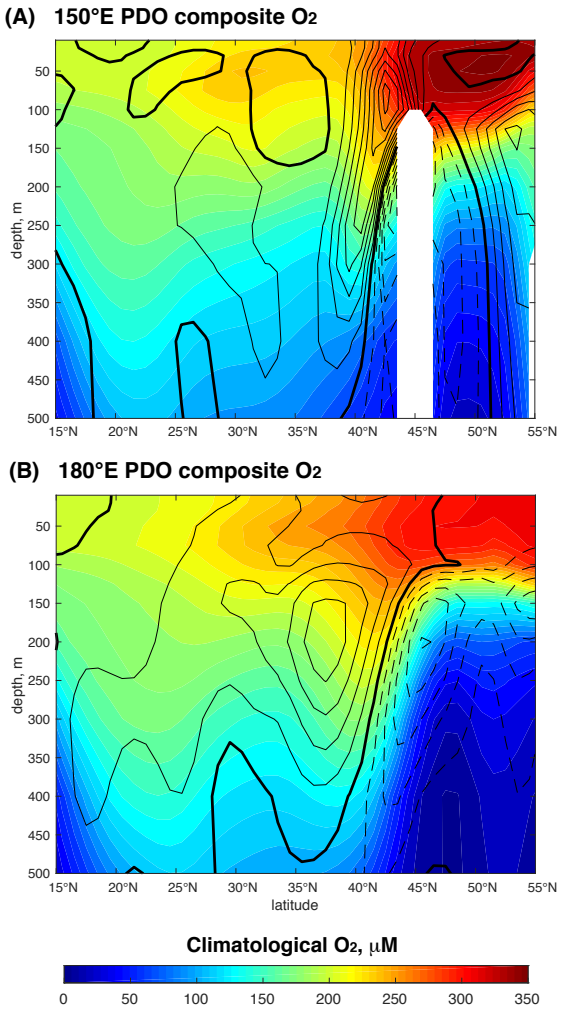

Figure 11. Simulated response of O_2 (A) at 150°E and (B) at 180°E in the North Pacific. Contour lines indicate O_2 anomalies associated with the PDO calculated by taking the difference between the positive and negative PDO composites. Black solid (dash) contours are positive (negative) O_2 anomalies with the interval of 5 μM. Color shading is the annual mean climatological O_2.

What mechanisms can explain the high correlation between $O_{2,heave}$ and O_2 while making the amplitude of O_2 variability significantly greater than that of $O_{2,heave}$? There is a possible biological effect that can reinforce the heave-induced O_2 changes [*Deutsch et al.*, 2011]. The low-latitude ecosystem is typically nutrient limited, and the isopycnal heave can modulate biological productivity through changing the position of nutricline with respect to the surface euphotic layer, thereby impacting O_2. Downward displacements of isopycnals moves the nutricline deeper in the water column, thereby curtailing nutrient supply to the euphotic layer; conversely, upward isopycnal displacements can enhance nutrient supply. Variations in biological production can modulate O_2 variability due to the respiration of organic matter at depth; a decrease in production associated with a downward isopycnal displacement alleviates subsurface oxygen demand, thereby reinforcing the direct effect of vertical advection on the background oxygen gradient.

The same analysis is performed at the depths of 100 and 400 m and results are shown in supplementary Figure S4 and S5. The analysis at 100 m shows greater regions of negative correlation especially outside of the tropics (supplementary Figure S4), indicating the important role of mixing and ventilation near the base of surface mixed layer. Also the regression coefficients exceed 1 more often at 100 m in the eastern tropical Pacific, because the relatively shallow oxycline there allows the heave effect to be well defined. The effect of isopycnal heave becomes more dominant at 400 m depth with a different spatial pattern (supplementary Figure S5). At this depth, the tropical-subtropical boundary and the subpolar regions are characterized by the regression coefficient of 1 or greater. The tropics are relatively noisy in the observations, but it appears that the relationship between O_2 and $O_{2,heave}$ is weaker at 400 m in the tropics likely because it is close to the core of the oxygen minimum zone where vertical gradient of O_2 and $O_{2,heave}$ vanishes.

5 Discussion and Conclusion

The superposition of anthropogenic trends and natural variability is a key issue that challenges the detection of human-induced biogeochemical changes [e.g., *Keller et al.*, 2014; *Long et al.*, 2016; *McKinley et al.*, 2016; *Rodgers et al.*, 2015; *Ito and Deutsch*, 2010]. However, natural variability is not just random "white" noise; rather, spatially coherent structures and preferred timescales arise from the dynamical nature of the coupled atmosphere-ocean system. This study focused on the aspect of O_2 variability associated with the PDO, a dominant mode of climate variability over the North Pacific with profound influences on the regional climate, marine ecosystem and fisheries [e.g. *Minobe*, 1997; *Mantua et al.*, 1997; *Chavez et al.*, 2003].

The PDO controls the basin-scale O_2 variability through at least two distinct mechanisms. The tropical O_2 variability is primarily set by the heave of isopycnals. Both model and observations show the zonal dipole of upper ocean O_2 associated with the changing thermocline depth. Analysis of modeled and observed O_2 anomalies revealed that the tropical O_2 variability cannot be fully explained by the vertical displacement of isopycnals. There is a possible biological effect that can reinforce the heave-induced O_2 changes [*Deutsch et al.*, 2011] where isopycnal heave can modulate biological productivity through changing the nutrient supply to the surface euphotic layer. In contrast, the subtropical O_2 variability is controlled by subduction. Elevated O_2 levels are found downstream of the deepened winter mixed layer consistent with a previous dynamical study [*Qu and Chen*, 2009]. These are distinct, independent mechanisms that are synchronized with the PDO time series.

While this study focused on the pattern of O_2 variability associated with PDO, there are other factors affecting biogeochemistry and O_2 in this region. *Mecking et al.* [2008] found no significant relationship between the PDO and O_2 at deeper depth. Similarly, *Di Lorenzo et al.* [2008] found no correlation between the PDO and O_2 observations in the

California Cooperative Oceanic Fisheries Investigations (CalCOFI) study region; O_2 in this region is significantly correlated with the North Pacific Gyre Oscillation (NPGO), which is the second mode of variability in North Pacific SST (or sea level height anomalies) [*Di Lorenzo et al.*, 2008]. Earlier studies suggested the role of lateral water mass shifts in controlling the low-frequency variability of O_2 and nutrient fields at mid latitudes [*Kwon et al.*, 2016b]. While we find the dominance of the vertical shifts in the tropics, we have not yet analyzed the effect of horizontal water mass shifts.

To conclude, we point out a few implications of this study. First, the ocean-ice configuration of the CESM-BGC, forced by the observed atmospheric states, is capable of reproducing the some features of the observed O_2 variability associated with the PDO. The climatological mean state of the model significantly underestimates the O_2 level of the tropical thermocline (Figure 1). This may be due to the underestimation of the ventilation of tropical thermocline; in this region, zonal ocean jets may play crucial roles in supplying O_2 to the poorly ventilated oxygen minimum zones [*Stramma et al.*, 2010], and the nominal 1° resolution of the model cannot adequately resolve these ocean jets. While the model is imperfect, however, it does capture some aspects of observed O_2 variability associated with the PDO (Figure 4) and we found the model useful in explaining some observed features of the O_2 changes. That said, this study is based on a single model forced by the observed atmospheric states, and simulated O_2 variability is at best moderately correlated with the observations. Thus, our results are subject to the biases in this particular model. A further study involving several different models is warranted to examine model-dependence and the robustness of the mechanisms suggested in this study [e.g. *Orr et al.*, 2017].

Our results have implications for interpreting local correlations between temperature and O_2. On the global scale, oceanic heat content and O_2 are negatively correlated in observations and models [*Keeling and Garcia*, 2002; *Keeling et al.*, 2010; *Ito et al.*, 2017]. Our results show that positive correlation between heat and O_2 is possible locally in the tropical thermocline. The heave-induced O_2 variability is linearly related to the potential density perturbations (Eq 3). Vertical gradients of O_2 and potential temperature are both positive in the tropical thermocline. Since the density is primarily controlled by the thermal component there, ρ_θ can be replaced with potential temperature (θ), leading to a positive correlation. This is consistent with the fact that recent expansion of the tropical Pacific OMZ is accompanied by a slight cooling [*Stramma et al.*, 2008] and shoaling thermocline [*Deutsch et al.*, 2014]. Since isopycnal heave itself only redistributes heat and O_2 within the ocean, it is not related to the global scale O_2-heat relationship.

Taken together, the evidence from the model and observations is consistent with the important role of PDO acting as a primary driver of natural variability. Even with model biases, the analysis of model outputs shows significant improvements in our understanding of the North Pacific O_2 and more broadly the mechanisms behind the large-scale O_2 variability. This merits additional scrutiny over the coming years; with higher resolution models, we should expect to see improved ocean dynamics including tropical thermocline ventilation with zonal jets, western boundary currents, subduction, and tracer stirring by mesoscale eddies, thus more realistic representation of mechanisms behind the O_2 variability and trends. The impacts of ocean deoxygenation on ocean ecosystems are profound and it is critical to develop improved understanding of the mechanisms driving trends and variability beyond the influences of PDO. In this light, the scientific community should work to ensure adequate observing capabilities and to strive for model improvements.

Acknowledgments
We are thankful for the support from the Scientific Visitor Program of the Climate and Global Dynamics Laboratory at the National Center for Atmospheric Research (NCAR) as this study started while the authors were visiting NCAR during the summer of 2016. NCAR is supported by the National Science Foundation. Computing resources (doi:10.5065/D6RX99HX)

were provided by the Climate Simulation Laboratory at NCAR's Computational and Information Systems Laboratory, sponsored by the National Science Foundation and other agencies. S.M. is supported by the Japan Society for the Promotion of Science (JSPS) KAKENHI (18H04129 and 18H04911). This project is supported by the National Science Foundation (1737188 to T.I., 1737282 to C.D., 1737158 to M.C.L.). All datasets supporting the conclusions of this study are available in the public domain as referenced within the paper. All of the data on which this manuscript is based is available from the corresponding author's institutional web server (http://shadow.eas.gatech.edu/~Ito/webdata/data.html).

References

Andreev, A. G., and V. I. Baturina (2006), Impacts of tides and atmospheric forcing variability on dissolved oxygen in the subarctic North Pacific, *J. Geophys. Res.*, *111*(C7), C07S10, doi:10.1029/2005JC003103.

Armstrong, R., C. Lee, J. Hedges, S. Honjo, and S. Wakeham (2002), A new, mechanistic model for organic carbon fluxes in the ocean based on the quantitative association of POC with ballast minerals, *Deep-Sea Res.*, *49*(1–3), 219–236, doi:10.1016/S0967-0645(01)00101-1.

Boyer, T., J. I. Antonov, O. K. Baranova, C. Coleman, H. E. Garcia, A. Grodsky, D. R. Johnson, R. A. Locarnini, A. V. Mishonov, T. O'Brien, C. Paver, J. Reagan, D. Seidov, I. V. Smolyar, and M. M. Zweng (2013), World ocean database 2013, in *NOAA Atlas NESDIS*, vol. 72, edited by S. Levitus and A. Mishonov, p. 209 pp, doi:10.7289/V5NZ85MT.

Brandt, P., V. Hormann, B. BourlèS, J. Fischer, F. A. Schott, L. Stramma, and M. Dengler (2008), Oxygen tongues and zonal currents in the equatorial Atlantic, *J. Geophys. Res.*, *113*, C04012, doi:10.1029/2007JC004435.

Brandt, P., R. J. Greatbatch, M. Claus, S.-H. Didwischus, V. Hormann, A. Funk, J. Hahn, G. Krahmann, J. Fischer, and A. KöRtzinger (2012), Ventilation of the equatorial Atlantic by the equatorial deep jets, *J. Geophys. Res.*, *117*, C12015, doi:10.1029/2012JC008118.

Breitburg, D., L. A. Levin, A. Oschlies, M. Grégoire, F. P. Chavez, D. J. Conley, V. Garçon, D. Gilbert, D. Gutiérrez, K. Isensee, and et al. (2018), Declining oxygen in the global ocean and coastal waters, *Science*, *359*(6371), eaam7240, doi:10.1126/science.aam7240.

Bretherton, C. S., M. Widmann, V. P. Dymnikov, J. M. Wallace, and I. Bladé (1999), The effective number of spatial degrees of freedom of a time-varying field, *J. Clim.*, *12*(7), 1990–2009, doi:10.1175/1520-0442(1999)012<1990:TENOSD>2.0.CO;2.

Cabré, A., I. Marinov, R. Bernardello, and D. Bianchi (2015), Oxygen minimum zones in the tropical Pacific across CMIP5 models: mean state differences and climate change trends, *Biogeosci.*, *12*(18), 5429–5454, doi:10.5194/bg-12-5429-2015.

Chavez, F. P., J. Ryan, S. E. Lluch-Cota, and M. Ñiquen C. (2003), From anchovies to sardines and back: Multidecadal change in the pacific ocean, *Science*, *299*(5604), 217–221, doi:10.1126/science.1075880.

Compo, G. P., J. S. Whitaker, P. D. Sardeshmukh, N. Matsui, R. J. Allan, X. Yin, B. E. Gleason, R. S. Vose, G. Rutledge, P. Bessemoulin, S. BrÃűnnimann, M. Brunet, R. I. Crouthamel, A. N. Grant, P. Y. Groisman, P. D. Jones, M. C. Kruk, A. C. Kruger, G. J. Marshall, M. Maugeri, H. Y. Mok, ï£¡. Nordli, T. F. Ross, R. M. Trigo, X. L. Wang, S. D. Woodruff, and S. J. Worley (2011), The twentieth century reanalysis project, *Quarterly Journal of the Royal Meteorological Society*, *137*(654), 1–28, doi:10.1002/qj.776.

Danabasoglu, G., S. C. Bates, B. P. Briegleb, S. R. Jayne, M. Jochum, W. G. Large, S. Peacock, and S. G. Yeager (2012), The CCSM4 Ocean Component, *J. Clim.*, *25*(5), 1361–1389, doi:10.1175/JCLI-D-11-00091.1.

Deutsch, C., S. Emerson, and L. Thompson (2006), Physical-biological interactions in North Pacific oxygen variability, *J. Geophys. Res.*, *111*, C09S90, doi: 10.1029/2005JC003179.

Deutsch, C., H. Brix, T. Ito, H. Frenzel, and L. Thompson (2011), Climate-Forced Variability of Ocean Hypoxia, *Science*, *333*, 336–339, doi:10.1126/science.1202422.

Deutsch, C., W. Berelson, R. Thunell, T. Weber, C. Tems, J. McManus, J. Crusius, T. Ito, T. Baumgartner, V. Ferreira, J. Mey, and A. van Geen (2014), Centennial changes in North Pacific anoxia linked to tropical trade winds, *Science*, *345*(6197), 665–668, doi: 10.1126/science.1252332.

Devries, T., and C. Deutsch (2014), Large-scale variations in the stoichiometry of marine organic matter respiration, *Nature Geosci.*, *7*, 890–894, doi:10.1038/ngeo2300.

Di Lorenzo, E., N. Schneider, K. M. Cobb, P. J. S. Franks, K. Chhak, A. J. Miller, J. C. McWilliams, S. J. Bograd, H. Arango, E. Curchitser, T. M. Powell, and P. Rivière (2008), North Pacific Gyre Oscillation links ocean climate and ecosystem change, *Geophy. Res. Lett.*, *35*, L08607, doi:10.1029/2007GL032838.

Dietze, H., and U. Loeptien (2013), Revisiting "nutrient trapping" in global coupled biogeochemical ocean circulation models, *Global Biogeochem. Cycles*, *27*, 265–284, doi: 10.1002/gbc.20029.

Duteil, O., F. U. Schwarzkopf, C. W. Böning, and A. Oschlies (2014), Major role of the equatorial current system in setting oxygen levels in the eastern tropical Atlantic Ocean: A high-resolution model study, *Geophy. Res. Lett.*, *41*, 2033–2040, doi: 10.1002/2013GL058888.

Eddebbar, Y. A., M. C. Long, L. Resplandy, C. Rödenbeck, K. B. Rodgers, M. Manizza, and R. F. Keeling (2017), Impacts of enso on air-sea oxygen exchange: observations and mechanisms, *Global Biogeochem. Cycles*, doi:10.1002/2017gb005630.

Emerson, S., Y. Watanabe, T. Ono, and S. Mecking (2004), Temporal Trends in Apparent Oxygen Utilization in the Upper Pycnocline of the North Pacific: 1980–2000, *J. Oceanogr.*, *60*(1), 139–147, doi:10.1023/B:JOCE.0000038323.62130.a0.

Garcia, H. E., and L. I. Gordon (1992), Oxygen solubility in seawater: Better fitting equations, *Limnology and Oceanography*, *37*(6), 1307–1312, doi:10.4319/lo.1992.37.6.1307.

Garcia, H. E., T. P. Boyer, S. Levitus, R. A. Locarnini, and J. Antonov (2005), On the variability of dissolved oxygen and apparent oxygen utilization content for the upper world ocean: 1955 to 1998, *Geophy. Res. Lett.*, *32*, L09604, doi: 10.1029/2004GL022286.

Garcia, H. E., R. A. Locarnini, T. P. Boyer, J. I. Antonov, A. V. Mishonov, O. K. Baranova, M. M. Zweng, J. R. Reagan, and D. R. Johnson (2014), World Ocean Atlas 2013, Volume 3: Dissolved Oxygen, Apparent Oxygen Utilization, and Oxygen Saturation, in *NOAA Atlas NESDIS 75*, edited by S. Levitus and A. Mishonov, p. 27 pp.

Getzlaff, J., and H. Dietze (2013), Effects of increased isopycnal diffusivity mimicking the unresolved equatorial intermediate current system in an earth system climate model, *Geophy. Res. Lett.*, *40*, 2166–2170, doi:10.1002/grl.50419.

Griffies, S., A. Biastoch, C. Böning, F. Bryan, G. Danabasoglu, E. Chassignet, M. England, R. Gerdes, H. Haak, R. Hallberg, W. Hazeleger, J. Jungclaus, W. G. Large, G. Madec, A. Pirani, B. L. Samuels, M. Scheinert, A. S. Gupta, C. A. Severijns, H. L. Simmons, A. M. Treguier, M. Winton, S. Yeager, and J. Yin (2009), Coordinated ocean-ice reference experiments (COREs), *Ocean Model.*, *26*(1-2), 1–46, doi: 10.1016/j.ocemod.2008.08.007.

Helm, K. P., N. L. Bindoff, and J. A. Church (2011), Observed decreases in oxygen content of the global ocean, *Geophy. Res. Lett.*, *38*, L23602, doi:10.1029/2011GL049513.

Huang, B., V. F. Banzon, E. Freeman, J. Lawrimore, W. Liu, T. C. Peterson, T. M. Smith, P. W. Thorne, S. D. Woodruff, and H.-M. Zhang (2015), Extended reconstructed sea surface temperature version 4 (ersst.v4). part i: Upgrades and intercomparisons, *Journal of Climate*, *28*(3), 911–930, doi:10.1175/JCLI-D-14-00006.1.

Ito, T., and C. Deutsch (2010), A conceptual model for the temporal spectrum of oceanic oxygen variability, *Geophy. Res. Lett.*, *37*, L03601, doi:10.1029/2009GL041595.

Ito, T., S. Minobe, M. C. Long, and C. Deutsch (2017), Upper ocean o2 trends: 1958âĂŞ2015, *Geophysical Research Letters*, *44*(9), 4214–4223, doi:10.1002/2017GL073613, 2017GL073613.

Kalnay, E., M. Kanamitsu, R. Kistler, W. Collins, D. Deaven, L. Gandin, M. Iredell, S. Saha, G. White, J. Woollen, Y. Zhu, A. Leetmaa, R. Reynolds, M. Chelliah, W. Ebisuzaki, W. Higgins, J. Janowiak, K. C. Mo, C. Ropelewski, J. Wang, R. Jenne, and D. Joseph (1996), The ncep/ncar 40-year reanalysis project, *Bulletin of the American Meteorological Society*, *77*(3), 437–471, doi:10.1175/1520-0477(1996)077<0437:TNYRP>2.0.CO;2.

Keeling, R. F., and H. E. Garcia (2002), The change in oceanic O_2 inventory associated with recent global warming, *Proc. Natl. Acad. Sci. U.S.A.*, *99*(12), 7848–7853, doi:10.1073/pnas.122154899.

Keeling, R. F., A. Körtzinger, and N. Gruber (2010), Ocean Deoxygenation in a Warming World, *Ann. Rev. of Mar. Sci.*, *2*, 199–229, doi:10.1146/annurev.marine.010908.163855.

Keller, K. M., F. Joos, and C. C. Raible (2014), Time of emergence of trends in ocean biogeochemistry, *Biogeosci.*, *11*(13), 3647–3659, doi:10.5194/bg-11-3647-2014.

Kwon, E. Y., C. Deutsch, S.-P. Xie, S. Schmidtko, and Y.-K. Cho (2016a), The North Pacific Oxygen Uptake Rates over the Past Half Century, *J. Clim.*, *29*(1), 61–76, doi:10.1175/jcli-d-14-00157.1.

Kwon, E. Y., Y. H. Kim, Y.-G. Park, Y.-H. Park, J. Dunne, and K.-I. Chang (2016b), Multidecadal wind-driven shifts in northwest pacific temperature, salinity, o2, and po4, *Global Biogeochemical Cycles*, *30*(11), 1599–1619.

Large, W., and S. Yeager (2009), The global climatology of an interannually varying air–sea flux data set, *Clim. Dyn.*, *33*(2–3), 341–364, doi:10.1007/s00382-008-0441-3.

Long, M. C., C. A. Deutsch, and T. Ito (2016), Finding forced trends in oceanic oxygen, *Global Biogeochem. Cycles*, *30*, doi:10.1002/2015GB005310.

Mantua, N. J., S. R. Hare, Y. Zhang, J. M. Wallace, and R. C. Francis (1997), A Pacific Interdecadal Climate Oscillation with Impacts on Salmon Production, *Bull. Amer. Meteor. Soc.*, *78*(6), 1069–1079, doi:10.1175/1520-0477(1997)078<1069:APICOW>2.0.CO;2.

McKinley, G. A., D. J. Pilcher, A. R. Fay, K. Lindsay, M. C. Long, and N. Lovenduski (2016), Timescales for detection of trends in the ocean carbon sink, *Nature*, *530*, 469–472, doi:10.1038/nature16958.

Mecking, S., C. Langdon, R. A. Feely, C. L. Sabine, C. A. Deutsch, and D.-H. Min (2008), Climate variability in the North Pacific thermocline diagnosed from oxygen measurements: An update based on the U.S. CLIVAR/CO_2 Repeat Hydrography cruises, *Global Biogeochem. Cycles*, *22*, GB3015, doi:10.1029/2007GB003101.

Minobe, S. (1997), A 50?70 year climatic oscillation over the north pacific and north america, *Geophysical Research Letters*, *24*(6), 683–686, doi:10.1029/97GL00504.

Moore, J. K., and O. Braucher (2008), Sedimentary and mineral dust sources of dissolved iron to the world ocean, *Biogeosciences*, *5*(3), 631–656, doi:10.5194/bg-5-631-2008.

Moore, J. K., S. C. Doney, and K. Lindsay (2004), Upper ocean ecosystem dynamics and iron cycling in a global three-dimensional model, *Global Biogeochem. Cycles*, *18*(4), GB4028, doi:10.1029/2004GB002220.

Moore, J. K., K. Lindsay, S. C. Doney, M. C. Long, and K. Misumi (2013), Marine ecosystem dynamics and biogeochemical cycling in the Community Earth System Model [CESM1(BGC)]: Comparison of the 1990s with the 2090s under the RCP4.5 and RCP8.5 scenarios, *J. Clim.*, *26*(23), 9291–9312, doi:10.1175/JCLI-D-12-00566.1.

Nakamura, T., T. Toyoda, Y. Ishikawa, and T. Awaji (2006), Effects of tidal mixing at the Kuril Straits on North Pacific ventilation: Adjustment of the intermediate layer revealed from numerical experiments, *J. Geophys. Res.*, *111*, C04003, doi:10.1029/2005JC003142.

Ono, T., T. Midorikawa, Y. W. Watanabe, K. Tadokoro, and T. Saino (2001), Temporal increases of phosphate and apparent oxygen utilization in the subsurface waters of western subarctic Pacific from 1968 to 1998, *Geophy. Res. Lett.*, *28*(17), 3285–3288, doi: 10.1029/2001GL012948.

Onogi, K., J. Tsutsui, H. Koide, M. Sakamoto, S. Kobayashi, H. Hatsushika, T. Matsumoto, N. Yamazaki, H. Kamahori, K. Takahashi, S. Kadokura, K. Wada, K. Kato, R. Oyama, T. Ose, N. Mannoji, and R. Taira (2007), The jra-55 reanalysis, *Journal of the Meteorological Society of Japan. Ser. II*, *85*(3), 369–432, doi:10.2151/jmsj.85.369.

Orr, J. C., R. G. Najjar, O. Aumont, L. Bopp, J. L. Bullister, G. Danabasoglu, S. C. Doney, J. P. Dunne, J.-C. Dutay, H. Graven, S. M. Griffies, J. G. John, F. Joos, I. Levin, K. Lindsay, R. J. Matear, G. A. McKinley, A. Mouchet, A. Oschlies, A. Romanou, R. Schlitzer, A. Tagliabue, T. Tanhua, and A. Yool (2017), Biogeochemical protocols and diagnostics for the cmip6 ocean model intercomparison project (omip), *Geoscientific Model Development*, *10*(6), 2169–2199, doi:10.5194/gmd-10-2169-2017.

Palter, J. B., and D. S. Trossman (2018), The sensitivity of future ocean oxygen to changes in ocean circulation, *Global Biogeochemical Cycles*, *32*(5), 738–751, doi: 10.1002/2017GB005777.

Qu, T., and J. Chen (2009), A north pacific decadal variability in subduction rate, *Geophysical Research Letters*, *36*(22), doi:10.1029/2009GL040914, l22602.

Rodgers, K. B., J. Lin, and T. L. Frölicher (2015), Emergence of multiple ocean ecosystem drivers in a large ensemble suite with an Earth system model, *Biogeosciences*, *12*(11), 3301–3320, doi:10.5194/bg-12-3301-2015.

Sasano, D., Y. Takatani, N. Kosugi, T. Nakano, T. Midorikawa, and M. Ishii (2015), Multidecadal trends of oxygen and their controlling factors in the western North Pacific, *Global Biogeochem. Cycles*, *29*, 935–956, doi:10.1002/2014GB005065.

Schmidtko, S., L. Stramma, and M. Visbeck (2017), Decline in global oceanic oxygen content during the past five decades, *Nature*, doi:10.1038/nature21399.

Stramma, L., G. C. Johnson, J. Sprintall, and V. Mohrholz (2008), Expanding Oxygen-Minimum Zones in the Tropical Oceans, *Science*, *320*, 655–658, doi: 10.1126/science.1153847.

Stramma, L., G. C. Johnson, E. Firing, and S. Schmidtko (2010), Eastern Pacific oxygen minimum zones: Supply paths and multidecadal changes, *J. Geophys. Res.*, *115*(C9), C09011, doi:10.1029/2009JC005976.

Whitney, F. A., H. J. Freeland, and M. Robert (2007), Persistently declining oxygen levels in the interior waters of the eastern subarctic Pacific, *Prog. Oceanogr.*, *75*, 179–199, doi:10.1016/j.pocean.2007.08.007.

Yeager, S. G., G. Danabasoglu, N. Rosenbloom, W. Strand, S. Bates, G. Meehl, A. Karspeck, K. Lindsay, M. C. Long, H. Teng, and et al. (2018), Predicting near-term changes in the earth system: A large ensemble of initialized decadal prediction simulations using the community earth system model, *Bull. Amer. Meteor. Soc.*, doi:10.1175/bams-d-17-0098.1.